Mode-selective Single-dipole Excitation and Controlled Routing of Guided Waves in a Multi-mode Topological Waveguide

Yandong Li,[1,*] Yang Yu,[1] Kueifu Lai,[2] Yuchen Han,[3]
Fei Gao,[4,5] Baile Zhang,[4,6] and Gennady Shvets[1,†]

[1]*School of Applied and Engineering Physics, Cornell University, Ithaca, New York 14853, USA*

[2]*Department of Physics, The University of Texas at Austin, Austin, Texas 78712, USA*

[3]*Department of Physics, Cornell University, Ithaca NY 14853, USA*

[4]*Division of Physics and Applied Physics, School of Physical and Mathematical Sciences, Nanyang Technological University, 21 Nanyang Link, Singapore 637371, Singapore*

[5]*Interdisciplinary Center for Quantum Information, State Key Laboratory of Modern Optical Instrumentation, ZJU-Hangzhou Global Science and Technology Innovation Center, College of Information Science and Electronic Engineering, Zhejiang University, Hangzhou 310027, China*

[6]*Centre for Disruptive Photonic Technologies, The Photonics Institute, Nanyang Technological University, 50 Nanyang Avenue, Singapore 639798, Singapore*

(Dated: November 12, 2021)

Topology-linked binary degrees of freedom of guided waves have been used to expand the channel capacity of and to ensure robust transmission through photonic waveguides. However, selectively exciting optical modes associated with the desired degree of freedom is challenging and typically requires spatially-extended sources or filters. Both approaches are incompatible with the ultimate objective of developing compact mode-selective sources powered by single emitters. In addition, the implementation of highly desirable functionalities, such as controllable distribution of guided modes between multiple detectors, becomes challenging in highly-compact devices due to photon loss to reflections. Here, we demonstrate that a linearly-polarized dipole-like source can selectively excite a topologically robust edge mode with the desired valley degree of freedom. Reflection-free routing of valley-polarized edge modes into two spatially-separated detectors with reconfigurable splitting ratios is also presented. An optical implementation of such a source will have the potential to broaden the applications of topological photonic devices.

I. INTRODUCTION

Photonic structures, such as waveguides, beam-splitters, and filters, represent an important family of optical components and devices that are crucial for compact (e.g., on-chip) generation and manipulation of light[1–3]. For optical communication applications, key characteristics of such components include bandwidth, reconfigurability, and channel capacity[4]. The latter can be enhanced by employing additional degrees of freedom (DoFs) of a light wave such as its polarization state or, in the case of a multi-mode waveguide, their mode index[5–7]. Additional DoFs of a photon can be utilized for various important tasks, including creating entangled states for quantum information science applications[8–10]. However, there are numerous challenges associated with using multi-mode waveguides. For example, different modes differ by their propagation speed, resulting in temporal separation between information-carrying pulses. In addition, preferential coupling to one specific mode often requires the emitter properties, such as the orientation of its dipole transition and its spatial

* yl2695@cornell.edu
† gs656@cornell.edu

location inside the waveguide, to largely match the electromagnetic profile of that mode and mismatch those of the others[11–13].

Topological photonics exploits symmetries in real and reciprocal spaces to enable robust propagation of edge (or kink) modes guided by domain walls between gapped photonic crystals with different quantized topological indices[14–16]. Examples of such topological indices associated with propagation bands include the Chern number[17,18] that can have nonzero integer values with broken time-reversal symmetry (TRS), as well as the spin-Chern[19–23] and the valley-Chern[24–28] half-integer indices in the systems with preserved TRS. Topological robustness associated with the latter Chern indices is contingent on the conservation of the corresponding binary DoFs: spin and valley DoFs, respectively. The synthetic spin DoF is preserved by the property of spin-degeneracy[19,21]; the valley DoF is preserved by the specific orientations of domain walls or photonic crystal terminations[24,25].

Therefore, topological photonics provides an entirely new way of thinking about propagation robustness, reflection suppression, and other empirically useful phenomena that can be engineered through preserving binary DoFs. For example, a domain wall between two photonic crystals with different topological indices can support topologically robust edge or kink (TREK) states. These TREK states are associated with conserved DoFs and do not suffer from back-scattering. Not surprisingly, advances in topological photonics have already contributed to conceptual developments in numerous photonic components and devices[29], including waveguides[26], cavities[30–33], and lasers[34–36]. Here we utilize the ideas from topological photonics to develop a new approach to mode-selective excitation of multi-mode robust waveguides by single (point-like) emitters. We also demonstrate reflection-free routing (or beam-splitting) of the excited modes into two spatially-separated detectors (see schematic in Fig. 1(b)) with reconfigurable splitting ratios. Unbalanced beam splitting has been proposed and used in several multi-photon non-classical interference experiments[37,38].

II. RESULTS

A. Description of the photonic platform

The multi-mode waveguide (MMW) is formed by the domain wall between two spin photonic crystals (SPCs) with opposite signed spin Chern number $C^{s,v}_{\mathrm{SPC}}$, where $s = \uparrow, \downarrow$

labels the binary spin DoF, and $v = K, K'$ labels the binary valley DoF. This MMW supports two forward-propagating ($s = \uparrow$) TREK states with identical group velocities, but different phase velocities corresponding to $v = K$ and $v = K'$[21–23]. The routing capability is enabled by placing a rhomboid-shaped valley photonic crystal (VPC) at the corner of the SPC domains. Domain walls between the band-gap-sharing SPC and VPC regions serve as single-mode waveguides supporting chiral TREK states labelled by their conserved spin and valley DoFs.

As a specific platform for realizing the SPCs and VPCs, we adopt the microwave photonic crystals introduced in Ref.[23] and used in several experiments[22,25]. The structure is comprised of an array of metallic rods arranged in a triangular lattice and placed between two metallic plates (at $z = \pm h/2$) which confines wave along the $\hat{z}$-direction. Non-trivial spin and valley textures are produced by breaking two distinct spatial symmetries[23]. Specifically, by placing the cylindrical rods asymmetrically with respect to the mid-height ($z = 0$) plane, the mirror symmetry is broken, and nonzero valley-independent photonic spin-Chern indices $C_{\mathrm{SPC}}^{\uparrow(\downarrow),v} = \pm\,\mathrm{sgn}(\Delta_s)/2$ are induced. Here the + (−) signs correspond to ↑ (↓) spin-polarized states and $\mathrm{sgn}(\Delta_s) = \mathrm{sgn}(g_{\mathrm{top}} - g_{\mathrm{bot}})$ [Fig. 1(a)], and $|\Delta_s| \propto (h - h_s)$ is proportional to the SPC band gap width (see Supplementary Material). Likewise, by modifying the rods' cross sections from circles to C_{3v}-symmetric tripod-like shapes, the in-plane inversion symmetry is broken, and nonzero spin-independent valley-Chern indices $C_{\mathrm{VPC}}^{s,K(K')} = \pm\,\mathrm{sgn}(\Delta_v)/2$ are induced. The + (−) signs correspond to $K(K')$ valley-polarized states. $|\Delta_v| \propto (\theta - 30°)$ [Fig. 1(a)] corresponds to the VPC band gap width (see Supplementary Material).

1. Propagation properties of TREK states

The bulk-edge correspondence predicts that, at SPC-VPC interfaces, only the TREK states with specific combinations of spin- and valley-DoFs exist[23,25,39]. As an example, we consider the SPC$^-$-VPC$^-$ interface [along the $\hat{x}$-direction in Fig. 1(c)]. Here the − sign represents $\Delta_s < 0$ ($\Delta_v < 0$) for SPC (VPC), respectively. For the subspace of electromagnetic modes with $s = \uparrow$ and $v = K'$, the difference between the Chern indices is $\Delta C = |C_{\mathrm{SPC}}^{\uparrow,K'} - C_{\mathrm{VPC}}^{\uparrow,K'}| = 1$, indicating that this interface supports one forward-propagating TREK state marked as $\Psi^{\uparrow K'}$ in Fig. 1(c), where $+\hat{x}$ is the forward direction. Similarly, the SPC$^+$-VPC$^-$ interface supports a $\Psi^{\uparrow K}$ TREK state propagating along the $-\hat{y}' = \hat{x}/2 - \sqrt{3}\hat{y}/2$

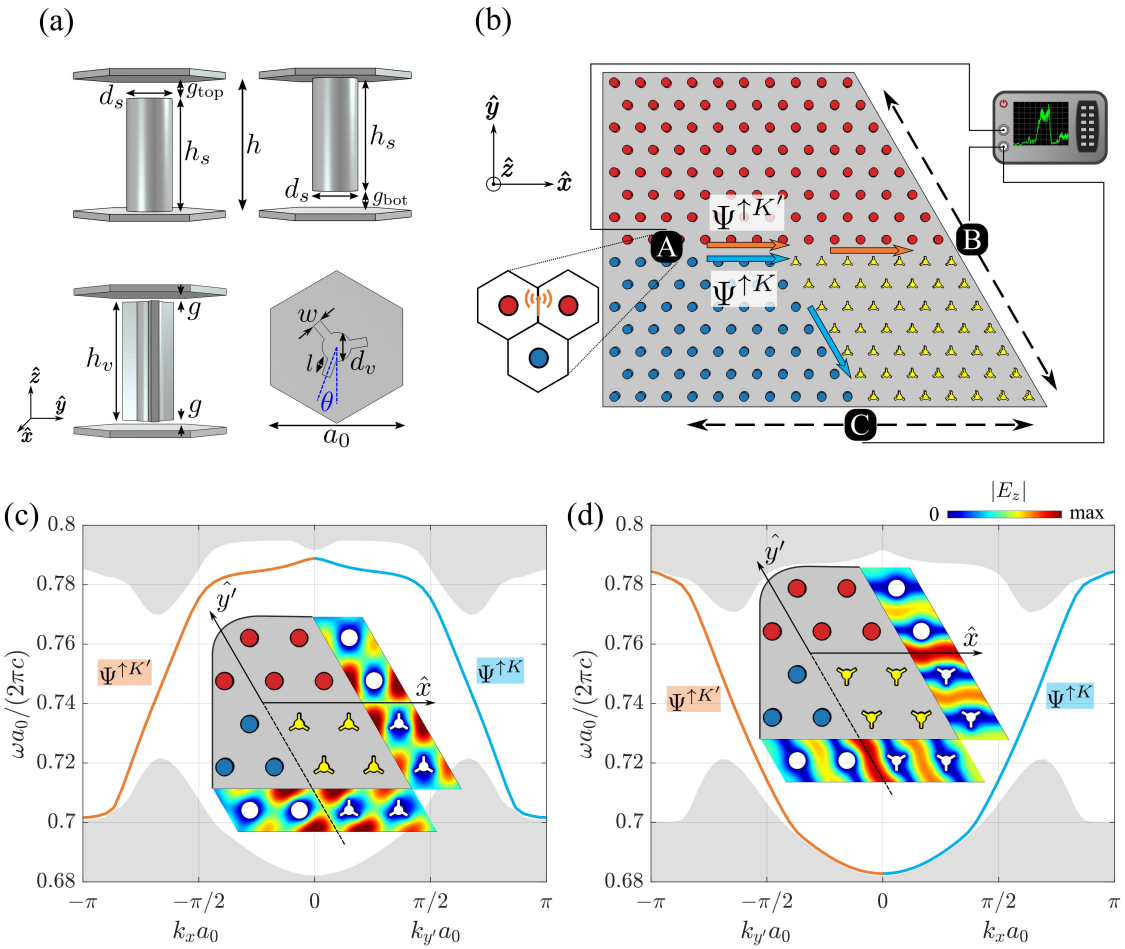

FIG. 1. (a) Geometrical definitions of the PTI unit cells. Upper left (right): SPC$^{+(-)}$ with $\Delta_s > 0$ ($\Delta_s < 0$). Lower left (right): VPC side (cross section) views. VPC$^{+(-)}$ configuration: $\Delta_v > 0$ when $\theta < 30°$ and $\Delta_v < 0$ when $\theta > 30°$. (b) Photonic structure for valley-selective splitting of the TREK states. Blue (red) circles: SPC$^{+(-)}$. Yellow tripods: VPC with $\theta = 60°$. A: valley-selective emitter embedded inside the MMW. B and C: receiving ports. Orange (cyan) arrow: $\Psi^{\uparrow K'}$ ($\Psi^{\uparrow K}$) TREK states. (c) Band diagrams of the two SPC-VPC interfaces from (b), for the tripods configuration $\theta = 60°$. Only the spin up states excited by emitter A in the SPC^{+}-SPC^{-} MMW are shown. Orange (cyan) solid lines: band-gap-spanning TREK states with $v = K'$ ($v = K$) valley DoF. Grey background: bulk modes. (d) Same as (c), but for the tripods configuration $\theta = 0°$. Insets: $|E_z|$ distributions of the TREK states at the corresponding SPC-VPC interfaces. Unit cell parameters: $d_s = 0.345a_0$, $h_s = 0.85a_0$, $g_{\text{top}} = g_{\text{bot}} = 0.15a_0$, $l = 0.12a_0$, $w = 0.06a_0$, $d_v = 0.2a_0$, $g = 0.03a_0$, $h_v = 0.94a_0$, $h = a_0$, where $a_0 = 36.8$mm is the lattice constant.

direction [Fig. 1(c)].

Propagation directions of such TREK states are exchanged by flipping the sign of Δ_v of VPC: the $\Psi^{\uparrow K}$ ($\Psi^{\uparrow K'}$) state propagates along the $+\hat{x}(-\hat{y}')$-direction [Fig. 1(d)]. For the specific VPC geometry shown in Fig. 1(a), such sign flip is accomplished by rotating the tripods. Therefore, the orientation angle θ of the tripods inside the VPC domain [Fig. 1(b)] can be used for valley-dependent splitting of electromagnetic energy: depending on θ, a given valley component predominantly flows into either port B or C.

Valley-dependent beam splitting using large VPC domains prevents the TREK states from evanescent tunnelling into an "unintended" port, and produces essentially $\sim 100\%$ flow into an "intended" port[39]. In contrast, when the VPC domain is a compact, "poor" insulator (with a narrow band gap), the tunnelling effect becomes significant. The finite size of the VPC region enables tunnelling of valley-polarized TREK states into the unintended port, thereby allowing the energy flow ratio to vary in a wide range. Using semi-analytical methods, we find that such change results from the considerable evanescent tunnelling when the band gap is narrow.

2. Launching valley-polarized TREK states

TREK states can be excited by feeding optical energy into the structure either from an external source[26] (e.g., through a waveguide) or directly by dipole-like emitters[25] embedded inside the topological MMW. The latter approach can potentially lead to more compact devices. However, exciting a spin-valley-polarized TREK state Ψ^{sv} with a specific combination of spin and valley DoFs (s, v) by a single emitter can be challenging. An arbitrarily placed point source (e.g., a single quantum emitter for the optical, or an electrically-small antenna for the microwave frequency range) will, in general, couple to multiple modes supported by the MMW. For example, a $\hat{z}$-polarized dipole placed inside a SPC$^+$-SPC$^-$ MMW generally radiates into all of the four TREK modes Ψ^{sv} modes, where $s = \uparrow, \downarrow$ and $v = K, K'$. For the TREK states excited by source A and travelling towards the beam splitter [indicated as the two arrows in Fig. 1(b)], the spin-DoF must be $s = \uparrow$. Although the sign of the group velocity automatically selects the spin-DoF, the valley-DoF is still undetermined.

While it is possible to block one of the two valley-polarizations by adding an extra filter to the structure[39], such an approach compromises compactness and completely prevents one

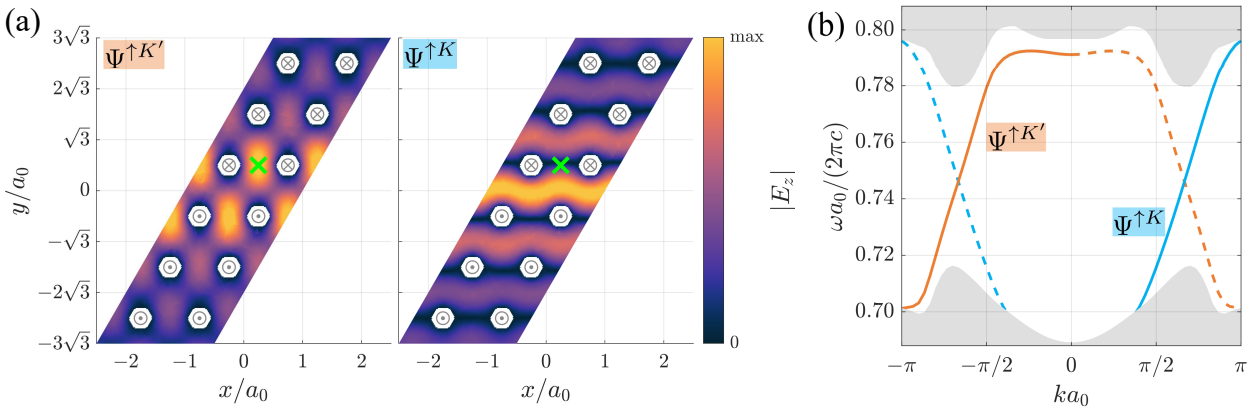

FIG. 2. TREK mode profiles and the photonic band structure of the SPC$^+$-SPC$^-$ MMW. (a) $|E_z|$ distribution of the $\Psi^{\uparrow K'}$ (left) and $\Psi^{\uparrow K}$ (right) TREK states in the mid-height ($z = 0$) plane at $\omega = \omega_0$. Green crosses: source position $\mathbf{r}_{K'}$ for selectively exciting the K'-valley-polarized state. Symbol $\otimes$ ($\odot$): rods attached to the top (bottom) plate. (b) Photonic band structure: bulk (grey shading) and TREK (solid and dashed lines) states. Solid orange (cyan) lines: forward-propagating $\Psi^{\uparrow K'}$ ($\Psi^{\uparrow K}$) states. Dashed lines: backward-propagating states moving away from the beam splitter. Parameters: same as in Fig. 1. Mid-gap frequency: $\omega_0 = 0.744\,(2\pi c/a_0)$.

of the two valley-polarized photons ($v = K$ or $v = K'$) from entering the beam splitter. An alternative approach to exciting the TREK state with a specific valley polarization utilizes precisely phased radiation sources[25,40]. However, this approach can hardly be compatible with the goal of developing single emitters for on-chip optical and potentially quantum information processing applications.

Here we demonstrate that a linearly-polarized dipole-like source can selectively excite valley-polarized TREK states propagating from the emitter towards the valley-dependent beam splitter. The latter can distribute such polarized states between two output ports in a controllable proportion. We place the emitter at a judiciously designed position based on the electromagnetic field distribution of the desired valley-polarized state. The $\hat{z}$-directional electric field distributions of the $\Psi^{\uparrow K'}$ and $\Psi^{\uparrow K}$ states are profoundly different [Fig. 2(a)], thus enabling valley-selective excitation of TREK states using a $\hat{z}$-directional electric dipole.

By placing the dipole source oscillating at frequency ω inside the band gap at the position $\mathbf{r}$ such that $|E_z^{\uparrow K'}(\omega, \mathbf{r})| \gg |E_z^{\uparrow K}(\omega, \mathbf{r})|$, we expect that the excitation efficiency $\Gamma^{\uparrow K'}(\omega) \propto |E_z^{\uparrow K'}(\omega, \mathbf{r})|^2$ of the $\Psi^{\uparrow K'}$ state is much larger than that of $\Psi^{\uparrow K}$ (see Supplementary Material for details). Specifically, when the dipole source is placed at the position $\mathbf{r} = \mathbf{r}_{K'}$ [Fig. 2(a)],

we find that $\Gamma^{\uparrow K'}/\Gamma^{\uparrow K} \approx 43$ at the mid-gap frequency $\omega = \omega_0 = 0.744\,(2\pi c/a_0)$. The high degree of valley selectivity can be verified by detecting the TREK states at the output ports B and C as described in Section II B below.

B. Realization of an unbalanced beam splitter for valley-polarized TREK states

1. Experimental results

All the metallic components for the photonic platform shown in Fig. 1 – round rods for the SPC, tripod-shaped rods for the VPC, and two plates – were constructed from aluminium. For the SPC, the round rods were directly attached to one of the two metal plates, so either one of the rod-plate gaps was set to zero ($g_{\rm top} = 0$ or $g_{\rm bot} = 0$). The tripods were symmetrically separated from both plates by foam (see Methods for details). The operating frequency $f \equiv \omega_0/2\pi \approx 6.1$GHz was set to the middle of the spectral band gap shared by SPC and VPC.

First, we experimentally validated the concept of valley-selective TREK launching at the SPC$^+$-SPC$^-$ domain wall in Sec. II A 2. This was done by placing a z-directional antenna between two rods in the SPC$^-$ domain adjacent to the SPC$^+$-SPC$^-$ domain wall, as shown in Fig. 2(a). Tunnelling through the VPC region was suppressed by selecting the tripods orientations, $\theta \equiv \theta_1 = 0^\circ$ and $\theta \equiv \theta_2 = 60^\circ$ to ensure the widest VPC band gaps. When the tunnelling is minimized, only one port (B for $\theta = \theta_2$ and C for $\theta = \theta_1$) is expected to receive the overwhelming majority of the K'-polarized radiation as illustrated by Figs. 1(c,d).

The tunnelling effect is quantified by introducing the power fluxes $W_{B(C)}$ captured by the corresponding port. The experimentally measured quantities $W^{\rm exp}_{B(C)}$ are obtained by scanning the pick-up antenna attached to the moving stage as shown in Fig. S7 of the Supplementary Material. The experimental beam-splitting ratio, defined as $R^{\rm exp}_C \equiv W^{\rm exp}_C/\left(W^{\rm exp}_C + W^{\rm exp}_B\right)$, is shown as circles in Fig. 3 for a range of tripod configuration angles. Specifically, $R^{\rm exp}_C \approx 0.87$ when $\theta = \theta_1$, and $R^{\rm exp}_B \equiv 1 - R^{\rm exp}_C \approx 0.89$ when $\theta = \theta_2$, confirming that the experimentally excited TREK state is indeed predominantly $\Psi^{\uparrow K'}$. We note that a backward-propagating $\Psi^{\downarrow K}$ TREK state of equal magnitude is also excited, because $\Psi^{\uparrow K'}$ and $\Psi^{\downarrow K}$ are time-reversal conjugates[23,41]. However, $\Psi^{\downarrow K(K')}$ propagates away from the VPC and cannot be measured by the detectors at port B or C.

For comparison, we simulated the structure with COMSOL and calculated the corresponding quantities $R_C^{\text{sim}} \equiv W_C^{\text{sim}} / \left(W_C^{\text{sim}} + W_B^{\text{sim}}\right)$ (green line in Fig. 3). $W_{B(C)}^{\text{sim}}$ is defined as $W_{B(C)}^{\text{sim}} \equiv \int\int_{B(C)} dS \langle W \rangle$, The surface integral is over the structural periphery at the corresponding port, and $\langle W \rangle$ is the time-averaged power flow perpendicular to that periphery. Simulation results are in good agreement with the experiment: $R_C^{\text{sim}} \approx 0.88$ when $\theta = \theta_1$, and $R_B^{\text{sim}} \equiv 1 - R_C^{\text{sim}} \approx 0.90$ when $\theta = \theta_2$. Note that a balanced beam splitter corresponds to $R_C = R_B = 0.5$, i.e., it splits energy of the incoming TREK state equally between the two ports.

An important conclusion from these findings is that, even though the tunnelling of the TREK states propagating towards their "intended" port into the "unintended" port is minimized by maximizing the VPC band gap for $\theta = \theta_{1,2}$, it cannot be entirely eliminated for a relatively compact beam-splitter used in this work. The tunnelling causes an effective "averaging" effect, lowering the received energy ratio $R_{C(B)}$ [for $\theta = \theta_{1(2)}$] below the excitation efficiency ratio $\Gamma^{\uparrow K'} / \left(\Gamma^{\uparrow K'} + \Gamma^{\uparrow K}\right) \approx 0.98$. This is because, with the maximized VPC band gap, the tunnelling is still not negligible in this finite-sized structure (see Supplementary Material for details).

As shown in Fig. 3, this tunnelling effect becomes more significant when the band gap narrows for $\theta_1 < \theta \leq \theta_g$ or $\theta_g \leq \theta < \theta_2$, where $\theta_g = 30°$ corresponds to the tripods orientation that closes the band gap. The experimentally measured and simulated beam splitting ratios change smoothly as θ approaches θ_g, and the band gap approaches zero. For example, when $\theta = 33°$, the exponential decay of the $\Psi^{\uparrow K'}$ state along the $-\hat{y}$-direction becomes significant (Fig. 3c), causing considerable amount of energy to tunnel to Port C. Below we develop a semi-analytical theory that describes how electromagnetic energy is distributed between the two ports in the presence of tunnelling.

2. Theoretical Model of Tunnelling

To quantitatively describe the tunnelling phenomena, we use the following ansatz to represent the $\Psi^{\uparrow K'}$ TREK state propagating along the SPC-VPC domain wall towards detector B:

$$\Psi^{\uparrow K'}(x, y, t) = \begin{cases} A e^{-i\omega t + (ik - \kappa_x)x} e^{-\kappa_2 y}, & \text{in the SPC domain,} \\ A e^{-i\omega t + (ik - \kappa_x)x} e^{\kappa_1 y}, & \text{in the VPC domain,} \end{cases} \tag{1}$$

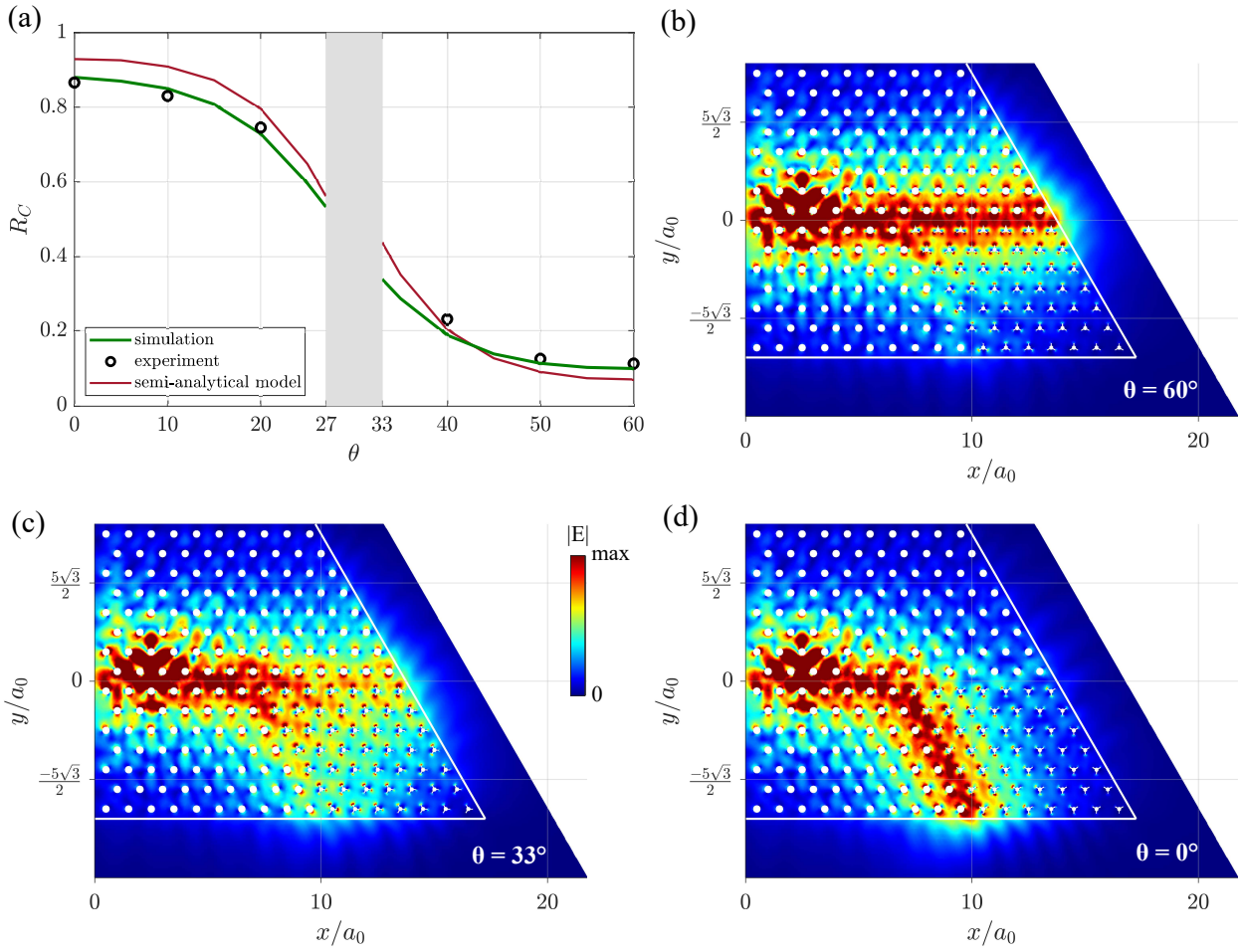

FIG. 3. (a) Beam-splitting ratio $R_C \equiv W_C/(W_C + W_B)$: experiment (black circles), COMSOL simulation (green lines), and semi-analytical theory (red lines). The VPC domain has no complete band gap for $27° < \theta < 33°$ (shadowed region). (b,d) Time-averaged energy density for the largest VPC band gap. Near-complete transmission of the $\Psi^{\uparrow K'}$ state to port B for $\theta = 60°$ ($\Delta_v < 0$) and to port C for $\theta = 0°$ ($\Delta_v > 0$). (c) Same as (b), but for a narrow VPC band gap for $\theta = 33°$. $R_C^{\text{sim}} \approx 0.34$. White lines: periphery of the metallic structure. The domain outside of the structure is free space.

for $x > x_0$ as defined in Fig. 4a. Here ω and k are the angular frequency and the wave-vector, respectively, and $\kappa_{1(2)}$ is the decay constant into the VPC (SPC) domain along the transverse ($\pm\hat{y}$) direction. The resulting tunnelling towards the structural periphery naturally leads to energy loss. Therefore, the amplitude of the TREK state also exponentially decays along its propagation $\hat{x}$-direction with the decay constant κ_x. Throughout this study, $\kappa_2 \equiv \kappa_2(\Delta_s)$ is a constant determined by the band gap width of the SPC. On the other hand, $\kappa_1 \equiv L_{\text{loc}}^{-1}(\Delta_v)$

implicitly depend on θ because $\Delta_v \equiv \Delta_v(\theta)$. As the VPC band gap narrows, $L_{\rm loc}$ increases.

Because κ_x and κ_1 are physically related to each other – finite κ_x is the consequence of the transverse directional tunnelling that happens when the wave propagates in the finite-sized structure along the longitudinal direction – we use a semi-empirical equation to relate κ_x and κ_1: $\kappa_x = \kappa_{x0} e^{-t/L_{\rm loc}}$ (see Supplementary Material for details). Here $\kappa_{x0} \approx 0.12/a_0$ and $t \approx 7.9 a_0$. The energy measured at port B (C), $W_{B(C)}$, is a sum of the *transmitted* energy $W_{\rm tr}$ and the *tunnelled* energy $W_{\rm tu}$:

$$\begin{aligned} &W_C = \Gamma^{\uparrow K'} W_{\rm tr} + \Gamma^{\uparrow K} W_{\rm tu},\ W_B = \Gamma^{\uparrow K} W_{\rm tr} + \Gamma^{\uparrow K'} W_{\rm tu}, \quad \text{for } 0^\circ < \theta < 30^\circ; \\ &W_C = \Gamma^{\uparrow K} W_{tr} + \Gamma^{\uparrow K'} W_{\rm tu},\ W_B = \Gamma^{\uparrow K'} W_{\rm tr} + \Gamma^{\uparrow K} W_{\rm tu}, \quad \text{for } 30^\circ < \theta < 60^\circ, \end{aligned} \tag{2}$$

where $W_{\rm tr}$ and $W_{\rm tu}$ depend on the decay constants κ_1, κ_2, and κ_x. Here $\Gamma^{\uparrow K'(K)}$ is the excitation efficiency of the $\Psi^{\uparrow K'(K)}$ state in the SPC$^+$-SPC$^-$ MMW.

With Eq. 2 and the decay constants calculated from the numerical results of COMSOL simulation (see Supplementary Material for details), we compute the ratio of energy that port C receives, R_C. The result [red curve in Fig. 3(a)] reveals the "averaging" effect due to band gap narrowing: the difference between W_B and W_C becomes smaller when θ approaches 30°. We note that the tripod configuration angles θ and $60^\circ - \theta$ correspond to the same VPC band gap width and hence the same $L_{\rm loc}$. Therefore, the semi-analytical result satisfies $R_B(\theta) = R_C(60^\circ - \theta)$. We focus on the energy ratio of the minor port [the one receives less energy, also see Fig. 4(b) caption], $\min(R_B, R_C)$.

Figure 4(b) demonstrates how $\min(R_B, R_C)$ depends on the excitation efficiency ratio $\Gamma^{\uparrow K'}/\Gamma^{\uparrow K}$ and the localization distance $L_{\rm loc}$ inside the VPC. By comparing the experimental results (filled dots) with the semi-analytical model (coloured background along the grey solid line), we observe that our model accurately captures how $\min(R_B, R_C)$ depends the localization length. Furthermore, Fig. 4(b) reveals that the high excitation selectivity grants considerable tunability of $R_{B(C)}$ for this compact structure.

The judiciously positioned dipole source provides an excitation efficiency ratio as high as $\Gamma^{\uparrow K'}/\Gamma^{\uparrow K} \approx 43$. With the high excitation selectivity of the $\Psi^{\uparrow K'}$ state, our semi-analytical model predicts that $\min(R_B, R_C)$ can change from 0.07 for $L_{\rm loc} = 3.4 a_0$ (insignificant tunnelling, high contrast between the two ports) to 0.20 for $L_{\rm loc} = 6.7 a_0$ (significant tunnelling, moderate contrast between the two ports). In experiment, as θ changes from 60° (corresponding to $L_{\rm loc} = 3.4 a_0$) to 40° (corresponding to $L_{\rm loc} = 6.7 a_0$), the energy ratio of the

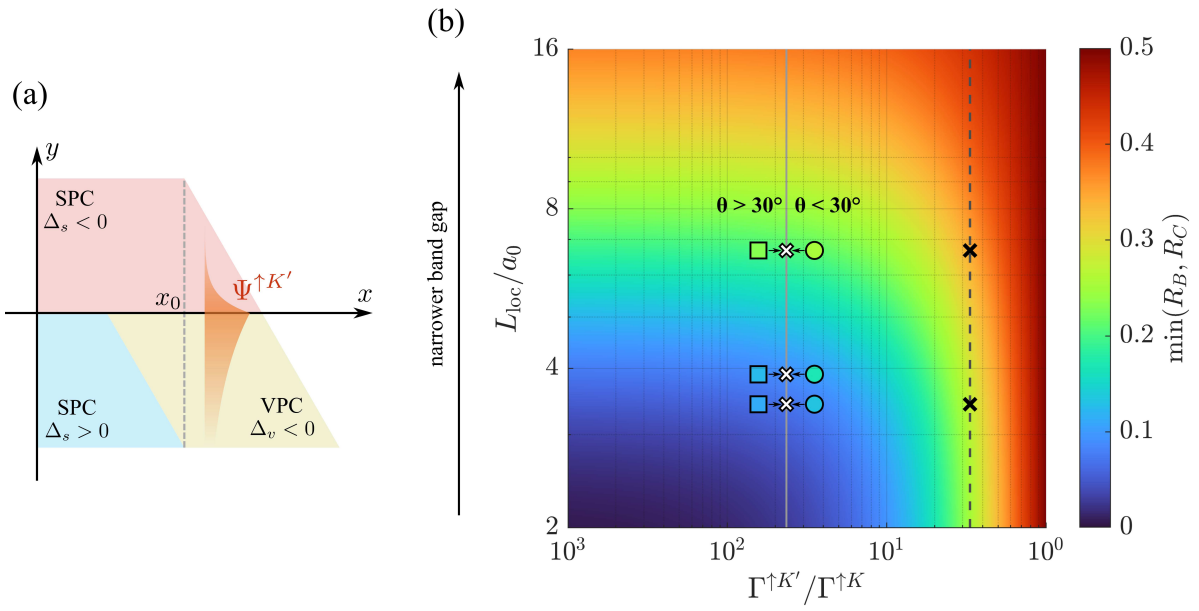

FIG. 4. (a) Schematic: leakage of the $\Psi^{\uparrow K'}$ state through the finite-sized VPC (yellow) region. Red and blue regions: SPCs with opposite signed spin-Chern numbers. (b) The beam-splitting ratio (colour-coded) of the minor port [port $B(C)$ for $0° < \theta < 30°$ ($30° < \theta < 60°$)]. High (low) contrast between the two ports occurs when $\min(R_B, R_C) \to 0$ [$\min(R_B, R_C) \to 0.5$]. Horizontal axis: valley-polarization selectivity of the excitation, $\Gamma^{\uparrow K'}/\Gamma^{\uparrow K}$. Vertical axis: localization distance $L_{\rm loc}$ of the TREK state inside the VPC, determined by the VPC band gap. Filled circles (squares): experimental data of $R_{B(C)}$ (filling-colour-coded) for $\theta = 0°$, $10°$, and $20°$ ($\theta = 40°$, $50°$, and $60°$), plotted to the right (left) of the grey vertical line which represents $\Gamma^{\uparrow K'}/\Gamma^{\uparrow K} \approx 43$, corresponding to the source shown in Fig. 2. The dashed black vertical line represents $\Gamma^{\uparrow K'}/\Gamma^{\uparrow K} = 3$ for comparison. The two black crosses label the maximum and minimum localization distances ($L_{\rm loc,max} = 6.7a_0$, $L_{\rm loc,min} = 3.4a_0$) that we implemented in experiment.

minor port is tuned from $R_C \approx 0.11$ to $R_C \approx 0.23$; as θ changes from $0°$ to $20°$, this ratio is tuned from $R_B \approx 0.13$ to $R_B \approx 0.25$. The result demonstrates that, for this compact structure, the energy received by the minor port can increase by $\sim 100\%$ as $L_{\rm loc}$ doubles. On the other hand, if the excitation selectivity was merely $\Gamma^{\uparrow K'}/\Gamma^{\uparrow K} \approx 3$, then, based on the semi-analytical result, $\min(R_B, R_C)$ can only be tuned from 0.27 to 0.34, i.e., only by $\sim 26\%$. As demonstrated in Fig. 4(b), the colour contrast along the dashed black line ($\Gamma^{\uparrow K'}/\Gamma^{\uparrow K} \approx 3$) is much less significant than that along the grey line ($\Gamma^{\uparrow K'}/\Gamma^{\uparrow K} \approx 43$). Overall, the high selectivity of the excitation enables the remarkable tunability of $R_{B(C)}$ for

this compact structure.

III. DISCUSSION

Channel capacity of optical communications devices can be expanded by employing multi-mode waveguides (MMWs). We demonstrate a new approach to manipulating the edge mode supported by a topological MMW. The waveguide is a sharp domain wall between two SPCs with opposite spin-Chern numbers, which supports two TREK states co-propagating with identical group velocities and distinguished by their binary valley DoFs. In addition to the topological robustness of the TREK states, we have demonstrated another important feature of this MMW: a single linearly-polarized emitter can excite, with high selectivity, only one of the two co-propagating TREK states. The high selectivity of excitation is verified by feeding the excited states into a compact junction of two topologically different SPC-VPC interfaces directed into separate output ports.

By controlling the band gap width of the VPC domain of the valley-DoF-sorter, it is possible to re-distribute the energy of a valley-polarized TREK state between the two output ports over a wide range: from $\sim 1:8$ to $\sim 1:3$, corresponding to the widest and the narrowest experimentally realized band gaps, respectively. We have presented a concise semi-analytical model to demonstrate that the physical reason for the energy re-distribution between the two output ports is evanescent tunnelling. We expect that future efforts to extend the concept of valley-based MMWs with single emitter source to the optical spectrum will benefit various applications from telecommunications to quantum information science.

IV. MATERIALS AND METHODS

A. Experiment and Simulation

The aluminum tripods used to build the VPC are fabricated using wire electrical discharge machining. Two pieces of structural foam (ROHACELL 51HF) are used to support the tripods between the two parallel plates. Another piece of structural foam with laser-cut holes is used for precisely locating the position and the directional angle of every tripod. The source is a 23mm long, $\hat{z}$-directional antenna.

We use a vector network analyzer (Keysight N5222A) to perform the measurement. Each set of measurement contains 257 transmission spectra taken at uniformly spaced positions r_i along periphery B or C of structure. To calculate the total amount of detected energy at a port, we sum $|S_{21}(r_i)|^2$ over all r_i along that periphery. The detect antenna is mounted on a motor-driven Velmex BiSlide rail. Electromagnetic wave absorbers are attached to one side of the rail to prevent reflection from the metallic surface (see Supplementary Material Fig. S7 for details).

We use the finite-element-frequency-domain software, COMSOL Multiphysics, to perform numerical computation. For band diagram calculations, we simulate supercells with 15 unit cells on both sides of the interface. All the metallic components are set as perfect electric conductors in COMSOL simulations.

B. Semi-analytical method

To analyse the TREK states, we solve the interface between two different Kane-Mele Hamiltonians,

$$\mathcal{H} = v(\delta k_x \hat{\tau}_z \otimes \hat{s}_0 \otimes \hat{\sigma}_x + \delta k_y \hat{\tau}_0 \otimes \hat{s}_0 \otimes \hat{\sigma}_y) + \Delta\mathcal{H}, \tag{3}$$

where $\delta\boldsymbol{k} = \boldsymbol{k} - \boldsymbol{K}$ or $\boldsymbol{k} - \boldsymbol{K}'$. $\hat{\tau}_i$, $\hat{s}_i$, and $\hat{\sigma}_i$ $(i = 0, x, y, z)$ are Pauli matrices acting on the band, spin, and valley subspaces. v represents the slope of the ungapped Dirac cone. The perturbation term is $\Delta\mathcal{H} \propto \Delta_s \hat{\tau}_z \otimes \hat{s}_z \otimes \hat{\sigma}_z$ for SPC and $\Delta\mathcal{H} \propto \Delta_v \hat{\tau}_0 \otimes \hat{s}_0 \otimes \hat{\sigma}_z$ for VPC. We obtain the decay constant $\kappa_{1(2)}$ by fitting an exponential function to the COMSOL-calculated time-averaged density profile of the TREK state (see Supplementary Material for details). The transmitted (tunnelled) energy, W_{tr} (W_{tu}), is calculated through evaluating $|\Psi^{\uparrow K'(K)}(x, y, t)|^2$ at the corresponding periphery of the structure.

ACKNOWLEDGMENTS

This work was supported by .

Author contributions

Y.L., K.L., and Y.H. carried out the experiment. Y.L. and Y.Y. performed the simulation. Y.L. provided theoretical analysis. F.G. and K.L. fabricated the sample. Y.L. and G.S. prepared the manuscript. G.S. and B.Z. supervised the project.

Data availability

The data are available at .

Conflict of interest

The authors declare that they have no conflict of interest.

---

[1] Bogaerts, W. *et al.* Programmable photonic circuits. *Nature* **586**, 207–216 (2020).

[2] Capmany, J. & Pérez, D. *Programmable Integrated Photonics* (Oxford University Press, 2020).

[3] Marpaung, D., Yao, J. & Capmany, J. Integrated microwave photonics. *Nature Photonics* **13**, 80–90 (2019).

[4] Agrell, E. *et al.* Roadmap of optical communications. *Journal of Optics* **18**, 063002 (2016).

[5] Yang, K. Y. *et al.* Inverse-designed multi-dimensional silicon photonic transmitters (2021). 2103.14139.

[6] Li, C., Liu, D. & Dai, D. Multimode silicon photonics. *Nanophotonics* **8**, 227–247 (2018).

[7] Bozinovic, N. *et al.* Terabit-scale orbital angular momentum mode division multiplexing in fibers. *Science* **340**, 1545–1548 (2013).

[8] Moody, G. *et al.* Roadmap on integrated quantum photonics (2021). 2102.03323.

[9] Bouchard, F. *et al.* Two-photon interference: the hong–ou–mandel effect. *Rep. Prog. Phys.* **84**, 012402 (2021).

[10] Mittal, S., Orre, V. V., Goldschmidt, E. A. & Hafezi, M. Tunable quantum interference using a topological source of indistinguishable photon pairs. *Nature Photonics* **15**, 542–548 (2021).

[11] Söllner, I. *et al.* Deterministic photon–emitter coupling in chiral photonic circuits. *Nature Nanotechnology* **10**, 775–778 (2015).

[12] Lodahl, P., Mahmoodian, S. & Stobbe, S. Interfacing single photons and single quantum dots with photonic nanostructures. *Rev. Mod. Phys.* **87**, 347–400 (2015).

[13] Rodriguez-Fortuno, F. J. *et al.* Near-field interference for the unidirectional excitation of electromagnetic guided modes. *Science* **340**, 328–330 (2013).

[14] Ozawa, T. *et al.* Topological photonics. *Rev. Mod. Phys.* **91**, 015006 (2019).

[15] Khanikaev, A. B. & Shvets, G. Two-dimensional topological photonics. *Nature Photonics* **11**, 763–773 (2017).

[16] Lu, L., Joannopoulos, J. D. & Soljačić, M. Topological photonics. *Nature Photonics* **8**, 821–829

(2014).

[17] Haldane, F. D. M. & Raghu, S. Possible realization of directional optical waveguides in photonic crystals with broken time-reversal symmetry. *Phys. Rev. Lett.* **100**, 013904 (2008).

[18] Wang, Z., Chong, Y. D., Joannopoulos, J. D. & Soljačić, M. Observation of unidirectional backscattering-immune topological electromagnetic states. *Nature* **461**, 772–775 (2009).

[19] Khanikaev, A. B. *et al.* Photonic topological insulators. *Nature Materials* **12**, 233–239 (2012).

[20] Chen, W.-J. *et al.* Experimental realization of photonic topological insulator in a uniaxial metacrystal waveguide. *Nature Communications* **5**, 5782 (2014).

[21] Ma, T., Khanikaev, A. B., Mousavi, S. H. & Shvets, G. Guiding electromagnetic waves around sharp corners: Topologically protected photonic transport in metawaveguides. *Phys. Rev. Lett.* **114**, 127401 (2015).

[22] Lai, K., Ma, T., Bo, X., Anlage, S. & Shvets, G. Experimental realization of a reflections-free compact delay line based on a photonic topological insulator. *Scientific Reports* **6**, 28453 (2016).

[23] Ma, T. & Shvets, G. Scattering-free edge states between heterogeneous photonic topological insulators. *Phys. Rev. B* **95**, 165102 (2017).

[24] Ma, T. & Shvets, G. All-si valley-hall photonic topological insulator. *New Journal of Physics* **18**, 025012 (2016).

[25] Gao, F. *et al.* Topologically protected refraction of robust kink states in valley photonic crystals. *Nature Physics* **14**, 140–144 (2018).

[26] Shalaev, M. I., Walasik, W., Tsukernik, A., Xu, Y. & Litchinitser, N. M. Robust topologically protected transport in photonic crystals at telecommunication wavelengths. *Nature Nanotechnology* **14**, 31–34 (2019).

[27] Dong, J.-W., Chen, X.-D., Zhu, H., Wang, Y. & Zhang, X. Valley photonic crystals for control of spin and topology. *Nature Materials* **16**, 298–302 (2017).

[28] Noh, J., Huang, S., Chen, K. P. & Rechtsman, M. C. Observation of photonic topological valley hall edge states. *Phys. Rev. Lett.* **120**, 063902 (2018).

[29] Ma, S. & Anlage, S. M. Microwave applications of photonic topological insulators. *Applied Physics Letters* **116**, 250502 (2020).

[30] Jin, J. *et al.* Topologically enabled ultrahigh-q guided resonances robust to out-of-plane scattering. *Nature* **574**, 501–504 (2019).

[31] Ota, Y. *et al.* Photonic crystal nanocavity based on a topological corner state. *Optica* **6**, 786–789 (2019).

[32] Gao, X. *et al.* Dirac-vortex topological cavities. *Nature Nanotechnology* **15**, 1012–1018 (2020).

[33] Li, Y., Yu, Y., Liu, F., Zhang, B. & Shvets, G. Topology-controlled photonic cavity based on the near-conservation of the valley degree of freedom. *Phys. Rev. Lett.* **125**, 213902 (2020).

[34] Harari, G. *et al.* Topological insulator laser: Theory. *Science* **359** (2018).

[35] Bandres, M. A. *et al.* Topological insulator laser: Experiments. *Science* **359** (2018).

[36] Zeng, Y. *et al.* Electrically pumped topological laser with valley edge modes. *Nature* **578**, 246–250 (2020).

[37] Cerf, N. J. & Jabbour, M. G. Two-boson quantum interference in time. *Proceedings of the National Academy of Sciences* **117**, 33107–33116 (2020).

[38] Sanaka, K., Resch, K. J. & Zeilinger, A. Filtering out photonic fock states. *Phys. Rev. Lett.* **96**, 083601 (2006).

[39] Kang, Y., Ni, X., Cheng, X., Khanikaev, A. B. & Genack, A. Z. Pseudo-spin–valley coupled edge states in a photonic topological insulator. *Nature Communications* **9**, 3029 (2018).

[40] Bo, X. *et al.* Exciting reflectionless unidirectional edge modes in a reciprocal photonic topological insulator medium. *Phys. Rev. B* **94**, 195427 (2016).

[41] F. Picardi, M., V. Zayats, A. & J. Rodríguez-Fortuño, F. Amplitude and phase control of guided modes excitation from a single dipole source: Engineering far- and near-field directionality. *Laser & Photonics Reviews* **13**, 1900250 (2019).